Construction and Building Materials 401 (2023) 132937

Contents lists available at ScienceDirect

Construction and Building Materials

journal homepage: www.elsevier.com/locate/conbuildmat

Effects of mineral wool waste in alkali activated-artificial aggregates for high-temperature applications

K.M. Klima [a,1], Y. Luo [a,1], H.J.H. Brouwers [a], Qingliang Yu [a,b,*]

[a] Department of the Built Environment, Eindhoven University of Technology, P.O. Box 513, 5600MB Eindhoven, the Netherlands
[b] School of Civil Engineering, Wuhan University, 430072 Wuhan, PR China

ARTICLE INFO

Keywords:
Mineral wool waste
Artificial aggregates
Geopolymer
High temperature

ABSTRACT

In this study, an alternative utilization route for Mineral Wool Waste (MWW) as a solid precursor for artificial aggregate manufacturing is proposed. The process parameters including alkali activation (Na or K) and curing regimes are investigated. Room and high-temperature (1000 °C) characterizations are performed on the plain aggregates and when incorporated in geopolymer composite. The results reveal that with an optimum pre-curing regime at room temperature for 3 days, artificial aggregates with particle density ranging from 1960 to 2090 kg/m^3 and crushing strength of 7.0 to 7.9 MPa can be obtained. The behaviour of aggregates is strongly related to the alkali cation type. The Na-based activator with high viscosity resulted in a more irregular grain shape with a lower particle density and a crushing strength as compared to K-activated aggregates. High crystallinity is observed in K-activated aggregates, causing better thermal stability. The alkali-activated artificial aggregates show a geopolymer-like behaviour in geopolymer composites, which contributes to higher strength development over normal sand aggregate.

1. Introduction

As one of the most utilized insulation materials for building energy conservation, mineral wool is applied either as thermal insulation [1] or acoustic material [2] in the shape of slabs, mats, or loose material placed into wall cavities [3]. A large amount of mineral wool waste (MWW) is formed during the manufacturing, construction and demolition operations. The MWW production in Europe was estimated to be 3 million tons by 2020, which is expected to further grow [4]. Its low density, low stiffness and poor compressibility lead to severe disposal problems from the aspects of toxic concerns, transportation, costs, and stability in landfills [5,6]. There have been different attempts to recycle MWW to reproduce ceramic products [7,8], fibre boards/panels [9,10] or reutilize it as fibre reinforcement/supplementary cementitious material in cement-based composites [11–13]. Unfortunately, due to its fibrous nature and inconsistency of the chemical/phase composition depending on the manufacturing process, the reutilization of MWW remains low [4]. Recently, Yliniemi et al. and Kinnunen et al. [14–17] suggested reutilizing MWW as a precursor for alkali-activated materials thanks to its favourable chemical, and mineralogical composition and high surface area for alkali activation. In alkali-activated MWW, the reaction product assemblage is mainly dependent on the type of mineral wool and activating solution chemistry, with aluminosilicate hydrates as the dominating phase. Among those, a promising mechanical performance is achieved, showing a compressive strength of up to 30.0 MPa for sole MWW-based alkali-activated material and 12.8 MPa for MWW/fly ash geopolymer composites. Nevertheless, one of the main drawbacks lies in the MWW-based binder is that a huge amount of alkali-activator is needed, which leads to the environmental issue [18]. In addition, the presence of organic resin in MWW such as phenolic resin, polyesters, and melamine-urea–formaldehyde may cause toxic volatile substances if the reutilization includes heating or chemical treatment [4,19]. In this case, developing alternative routes for the large quantity valorisation of MWW is crucially needed, especially considering cost-efficiency and eco-friendliness.

In the last decades, the utilization of waste materials, such as recycled concrete, furnace bottom ash, GGBFS, or fly ash as raw material in making artificial aggregate (AA) is a subject of growing interest. It not only helps to tackle the disposal problem with waste and industrial by-products but also eases the high demand and limited supply of natural aggregates [20,21]. Up to now, the design of artificial aggregate solely based on MWW has not been reported. López-García et al. [22] for the

* Corresponding author at: Department of the Built Environment, Eindhoven University of Technology, P.O. Box 513, 5600MB Eindhoven, the Netherlands.
E-mail address: q.yu@bwk.tue.nl (Q. Yu).
[1] These Authors contribute equally to this work.

https://doi.org/10.1016/j.conbuildmat.2023.132937
Received 9 June 2023; Received in revised form 12 July 2023; Accepted 9 August 2023
Available online 15 August 2023

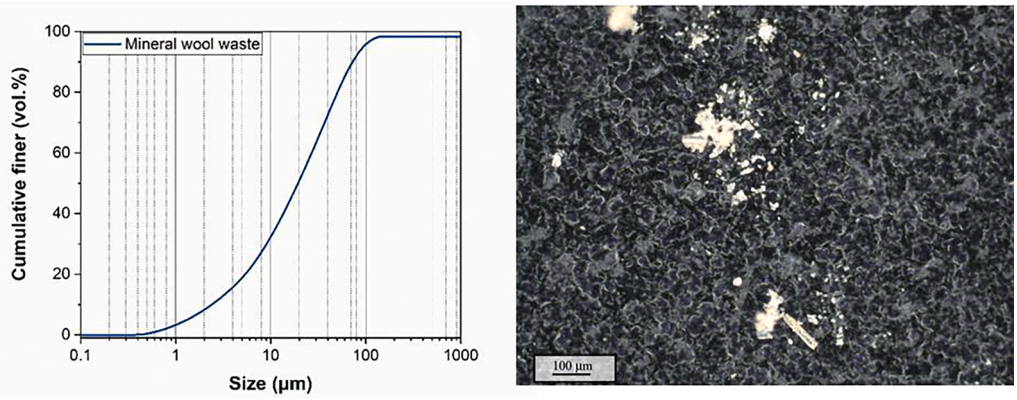

Fig. 1. Particle size distribution of waste material and the visual representation of MWW after milling.

Table 1
Chemical composition of mineral wool waste (MWW) and fly ash (FA).

Content (%)	SiO_2	Al_2O_3	CaO	Fe_2O_3	MgO	K_2O	SO_3	TiO_2	V_2O_5	Cr_2O_3	MnO	Others	LOI	Si/Al (mol/mol)
MWW	37.6	17.5	19.6	9.9	7.8	1.3	0.3	1.9	0.1	0.1	0.4	0.2	3.5	1.82
FA	54.5	21.5	6.1	9.1	1.3	2.8	0.4	1.3	–	–	–	0.9	2.0	–

first time applied mineral wool as a component in the manufacture of lightweight aggregates. Due to the poor plasticity and workability of mineral wool in a water system, a supplementary sepiolite was incorporated, and an extrusion-firing process was applied to achieve a mechanical strength of 2–6 Mpa. As discussed above, owing to the certain reactivity of MWW under alkaline environment, alkali activator can be used as moisture agent to optimize the workability and reinforce the bonding among MWW, makes it possible to prepare AA solely based on MWW. Moreover, with the spraying technology, the pelletizing process could largely reduce the necessary moisture content, easing the demand of alkali-activator. However, to the best of the authors' knowledge, there is an absence of information concerning the application of fibrous MWW in the process of making AA via alkali activation. The effect of manufacturing parameters, especially the alkali cation, and curing regime on the properties of obtained AA should be further determined.

In addition, as an eco-friendly alternative binder to ordinary Portland cement (OPC), alkali-activated binders are known to exhibit promising high-temperature resistance over OPC-based materials [23]. Nevertheless, little information is available on making high-temperature resistant artificial aggregates based on alkali-activated materials. Up to now, lightweight aggregate (LWA) is most commonly used for high-temperature resistance, such as pumice, perlite, vermiculite, expanded perlite and clay, etc. [24–26]. However, the intrinsically high cost due to the specific fabrication process as well as their insufficient mechanical strength because of the porous structure largely restrict their large-scale application. Moreover, the inclusion of these aggregates in alkali-activated binders always results in dramatically declined mechanical strength due to the different thermal expansion behaviour between geopolymer and aggregates during high-temperature exposure [27,28]. In this case, alkali-activated MWW aggregates could be a promising alternative to commercial lightweight aggregates. On the one hand, given its mineral composition and manufacturing method, MWW equips itself with good thermal stability [29], on the other hand, the MWW-based binder after alkali activation has promising high-temperature resistance and exhibits similar thermal behaviour to other alkali-activated binders. Nevertheless, there is a lack of comprehensive understanding on the thermal behaviour of artificial aggregates when they are exposed to high temperatures, as well as the interaction between alkali-activated artificial aggregates and either cement or geopolymer systems under elevated temperatures remains unknown.

The goal of this work is to design alkali-activated aggregates based on MWW, combined with the characterization of basic properties and thermal stability up to 1000 °C. The role of alkali cation (Na or K), and curing regime are discussed and recommendation based on the material performance are provided. A significantly lower curing temperature of 800 °C is applied as compared to that normally used in the manufacture (around 1200 °C) to remove organic resin [30], immobilize heavy metals [31] and improve thermal stability. Basic room temperature properties including particle shape morphology, water absorption, particle density, and crushing strength of the obtain aggregate materials are determined. Thermogravimetric analysis, contour microscopy, and in-situ high-temperature XRD analyses are carried out to establish the suitability of aggregates for high-temperature applications and predict their behaviour when applied in the mortar. Lastly, the manufactured aggregates are incorporated into the alkali-activated binder (geopolymer), and their performance at room temperature and after exposure to 1000 °C are investigated and compared with commonly used sand aggregates. Based on this, the bonding behaviour, mechanical characteristics, and high-temperature responsiveness of the artificially fabricated aggregates are clarified, and these aspects are further correlated with the high temperature behavior of the geopolymer mortar. This work validates the potential of alkali activation of MWW for the purpose of manufacturing artificial aggregate and proposes a guideline for further research towards reutilization strategy for MWW.

2. Materials and methods

2.1. Raw materials

In this experiment, mineral wool waste (MWW) was employed as the raw material. The waste was provided by Rockwool B.V., consisting of the waste material from the fine processing and crushed final products. It is a light material with a cured organic binder. The obtained MWW was processed using a disc mill (Retsch Vibratory Disc mill RS200) to reach the required particle size. The particle size distribution of raw materials was assessed using a laser particle size analyser (Mastersizer 2000, Malvern Instruments, UK), as shown in Fig. 1. On the black background, the bright (yellowish) part represents mineral wool waste. As can be seen, the material is inhomogeneous, with different particle shapes after milling, with some being more spherical and others remaining elongated or fiber-like.

The average particle size (d_{50}) of MWW was 20.2 μm. The chemical

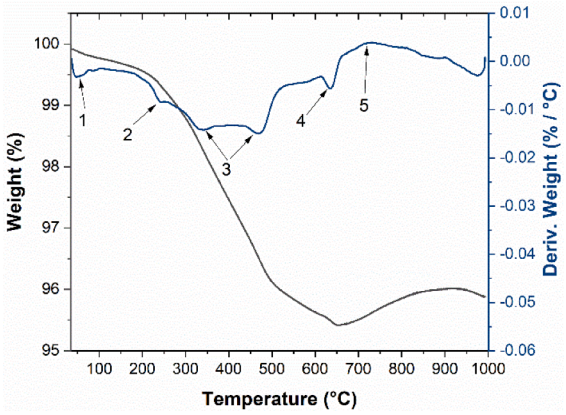

Fig. 2. TG-DTG results of raw MWW. 1) Water release present in sizing agent and at the surface [32]; 2) 240 °C the burning of organic binder and dust binding oil in the sample; 3) oxidation of the pyrolysis residues from binder [33]; 4) the binder evaporation at 650 °C [33]; 5) the oxidation of Fe^{2+} to Fe^{3+} [34].

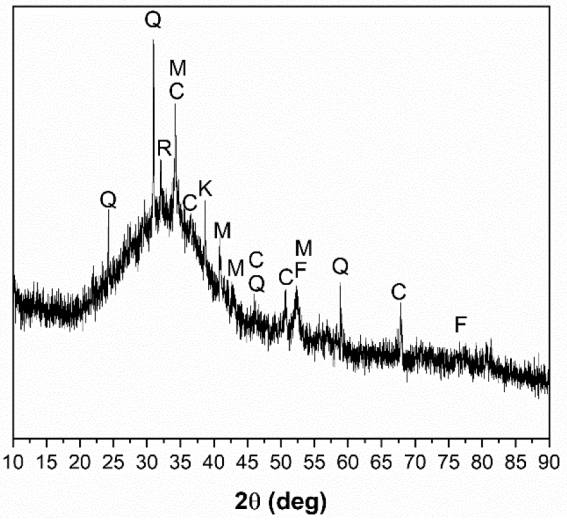

Fig. 3. XRD diffractograms of raw material. Legend: Q: Quartz; R: Rutile; C: Calcite; K: Potassium aluminium silicate ($K_{1.25}Al_{1.25}Si_{0.75}O_4$); F: Ferrite; M: Magnesium Aluminium Silicate (Pyrope $Mg_3Al_2(SiO_4)_3$).Motivation for the selected utilization method.

Table 2
Mix details of manufactured aggregates.

Sample code	Alkali cation	Relative humidity (%)	Curing regime Temp (°C)	Time (day)
Na20-1	Sodium		20	1
Na20-2	Sodium	80	20	2
Na20-3	Sodium		20	3
K20-1	Potassium		20	1
K20-2	Potassium	80	20	2
K20-3	Potassium		20	3
Na50-1	Sodium		50	1
Na50-2	Sodium	80	50	2
Na50-3	Sodium		50	3
K50-1	Potassium		50	1
K50-2	Potassium	80	50	2
K50-3	Potassium		50	3

composition was measured using X-ray fluorescence spectrometry (XRF) (PANalytical Epsilon 3), and the loss on ignition was calculated using the mass difference after firing at 1000 °C.

The chemical composition as well as the loss on ignition of MWW is shown in Table 1. TGA of raw material was carried out in an air environment between 30 and 1000 °C with a step of 20 °C/min, and Fig. 2 depicts the TG-DTG results with a brief description of temperature-induced events. The purpose of TGA was to clarify the thermal stability of MWW and establish the minimum sintering temperature required to remove the contained organic binder. Recent developments in artificial aggregate production have shown that sintering consumes energy at temperatures beyond 1000 °C. The TGA results supported by Ivanič et al. [32] confirmed that the combustion of the binder and other organic hydrophobic substances resulted in weight loss up to 800 °C. Thus, this study proposed an 800 °C alkali activation process that is cost-effective, practical, easy to use, and environmentally benign as compared to the traditional artificial aggregate production process.

Sodium and potassium-based activators have gained considerable recognition in the field of Alkali-Activated Materials (AAMs) and have been extensively researched. The selection of alkali activator plays a pivotal role in determining the properties of AAMs. Sodium and potassium-based activators exhibit distinct chemical properties and their interaction with precursor materials can lead to variations in microstructure, strength, setting time, workability, and other crucial properties of AAMs. These activators offer the advantage of cost-effectiveness and widespread availability, as sodium and potassium are abundant elements that can be sourced from diverse natural and industrial sources.

To prepare the activator solutions, an alkali activating solution was formulated using analytical-grade NaOH and KOH pellets (with a purity of 99 wt%), a commercial sodium silicate solution (containing 8.4% Na_2O, 27.7% SiO_2, and 63.9% H_2O), and potassium silicate (comprising 8% K_2O, 20.8% SiO_2, and 72.8% H_2O). The activator solutions were tailored to achieve a consistent silica modulus of 1.5 and a fixed oxide content of 6% M_2O (where M = Na, K), calculated as molar equivalents based on dry solids. Distilled water was utilized in the preparation of the solution.

The amorphous character of the initial material was disclosed through XRD phase analysis (Fig. 3). Trace amounts of crystalline phases were detected, such as quartz and calcite, in agreement with Pavlin et al. [35]. Furthermore, the presence of iron was confirmed, which occurs in a divalent state owing to the reducing conditions of material production. The presence of aluminosilicates (magnesium and potassium) is the consequence of the basic composition of stone wool fibre, which is manufactured from an aluminosilicate rock mixture (usually basalt).

2.2. Preparation of Samples: Aggregates and mortar

2.2.1. Aggregates manufacturing

Aggregates were produced by applying an agglomeration process using an Eirich-type GTE disc pelletizer. The settings were 150 rpm and a slope of 45°. First, the mineral wool waste powder was added to the pan, followed by alkali activator spraying until the surface was moist. Last, the dry powder of MWW was re-applied to promote agglomeration and aggregate formation. Finally, due to gravity and pan movement, the granules that had attained a stable shape dropped out of the pan, indicating the end of the production. Following that, moist granules were cured in the environment chamber at RH80% at varied temperatures and times (Table 2).

The cured aggregates were sieved (<125 μm) to remove small-size particles before being sintered at 800 °C for 2 h. The sintering was introduced to remove residual organic resin and increase the reactivity of unreacted particles [36]. The aggregates were stored in sealed plastic bags until further testing.

2.2.2. Geopolymer mortar design

In this work, the geopolymer-based mortars were prepared by applying fly ash (FA) (Chemical composition in Table 1) as the binder material, and three size fractions of mineral wool waste-based aggregate

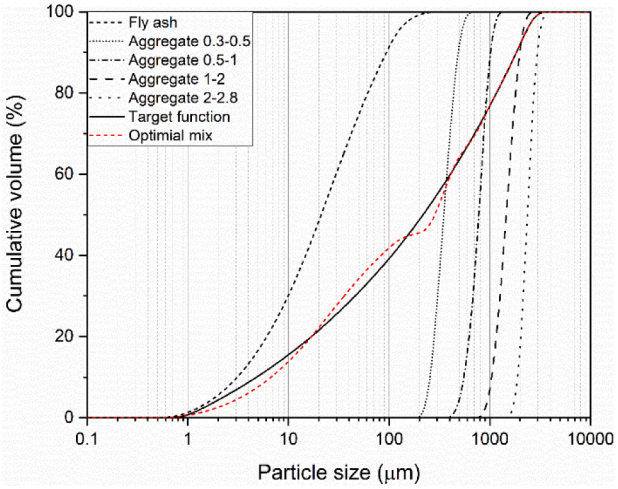

Fig. 4. Particle size distributions of the raw materials, the target curve and the resulting integral grading line of a sample mix.

Table 3
Mix proportions of geopolymer composites (kg/m^3).

Mix	Fly ash	Activator	Agg 0.3–0.5	Agg 0.5–1	Agg 1–2	Agg 2–2.8
K	790.8	404.2	173.5	164.6	221.4	121.5
Na	790.7	404.2	169.1	158.8	217.9	119.3
Sand	790.8	332.1	365.5	226.1	276.6	150.3

were used. The particle size distribution of each fraction is shown in Fig. 4. The alkaline solution for the geopolymer was obtained by combining potassium hydroxide pellets (VWR Life Science, reagent grade) and potassium silicate solution (WHC GmbH, K_2O 8%, SiO_2 20%, 72.8 % H_2O by mass) to achieve a SiO_2/K_2O ratio of 1.4. To ensure an adequate number of specimens for both room temperature mechanical testing and high-temperature shrinkage and mechanical strength evaluation, six prism specimens with dimensions of 160x40x40 mm^3 per mix design were prepared.

The geopolymer mortar was designed based on the modified Andreasen & Andersen particle packing model [37]:

$$P(D) = \frac{D^q - D_{min}^q}{D_{max}^q - D_{min}^q} \quad (1)$$

In which P(D) is the cumulative fractions of particles smaller than D. D_{max} and D_{min} represent the maximum and minimum particle size, respectively. q is the distribution modulus. Brouwers [38,39] suggested that the positive effect can be obtained with a q-value range of 0–0.37. Gao et al. [40], Borges et al. [41] and Ng et al. [42] recommended a q value in a range of 0.20–0.26 for a geopolymer-based binder. In this study, a q value of 0.2 was adopted to achieve good workability and packing without using any superplasticizers. Based on that, the calculated target function curve and the fitted grading curve are shown in Fig. 4, and the detailed mix proportions are listed in Table 3. In order to make the results comparable, in the mixtures with different types of aggregates, the volume of each size fraction for different aggregates was kept constant. Moreover, as suggested by Yliniemi et al. [43], the aggregates used in geopolymer composites were not pre-wetted prior to mixing to establish a favourable ITZ between the fresh paste and the rough, porous grain surface. The amount of water was design to ensure good workability of the composite. It should be noted that due to the more irregular shape of Na-based aggregates, a slightly lower flowability is noticed in geopolymer mortar with incorporated Na-based aggregates. Two best performing aggregates material were used for this investigation and compared to commercially available sand (coarse industrial sand used in floor mortars).

2.3. Characterization methods

Geopolymer and aggregate analysis involve the utilization of diverse tests and methods to thoroughly evaluate and understand the properties and distinctive characteristics of these materials.

2.3.1. Characterization of aggregates

Viscosity Measurement: The viscosity of two activator solutions was measured using a stress/strain controlled rotational rheometer (Anton Paar MCR501) in couette configuration. Each solution was tested twice at a temperature of 20 °C with 21 data points per measurement.

Density, porosity; By following the guidelines of ASTM C128-01 [44], three basic parameters of the artificial aggregates were evaluated, namely:

Water absorption defined as the increase in aggregate mass caused by water accessing the pores of the particles during a certain time. The particle density ρp (kg/m^3) is oven-dry mass of aggregate per unit volume of aggregate particles, including permeable and impermeable pores but excluding spaces between particles. The apparent density ρa (kg/m^3) is the mass per unit volume of the impermeable portion of the aggregate particles. The volume fraction of the open porosity that is interconnected is calculated as follows [45]:

$$V_{open} = 1 - \frac{\rho_p}{\rho_a}$$

Where ρp corresponds to the bulk density of the aggregate grain and ρa refers to the apparent specific density which defines the mass of a volume of the impermeable portion of a material at a stated temperature.

Mechanical performance: According to [46], the single crushing strength of aggregates was performed using a crushing testing machine recording the failure load (P) and the diameter of the aggregate (x) and presented as an average value per batch and calculated as follows [47]:

$$\sigma = \frac{2.8^*P}{\pi^* x^2} \quad (3)$$

High-Temperature In-situ XRD: To determine the mineralogical transformation of raw materials and aggregates exposed to high temperatures up to 1000 °C, high-temperature in-situ X-ray diffraction (XRD) was performed. The measurements were conducted using an X'Pert Pro PANalytical diffractometer with a Co X-ray tube in theta-theta geometry. Corundum served as an external standard. The samples were measured in the range of 10-70° 2θ with a step size of 0.039° 2θ and a time per step of 40.9 s.

FactSage is the application used for the calculations the equilibrium phase assemblage of a given chemical composition using a Gibbs-Free Energy minimization calculation [50].The application works with the FACTPS database of pure chemicals, which contains all of the thermodynamic properties of these pure substances. The application makes use of databases containing models for solution phases. Solids (solid solutions) or melts can be used. It has been estimated the stable phase assemblage in the discussed scenario utilising the database CON2, which comprises various solid solution models. Clinopyroxene, melilite, Ti-spinel, olivine, leucite, and nepheline were the six solid solution phases included in the computation. Other components that may be present in a pure phase were dealt with by the solution models. As a result, the computation was set up as MWW + activator increments (with modulus = 1.5), and the equilibrium phases assembly was determined for each incremental addition.

The microstructure of aggregate morphology and its distribution within the geopolymeric matrix were analyzed using a ZEISS Axio Imager coupled with a ZEISS Axiocam 305 CAMERA Colour, Z2 optical microscope (Carl Zeiss, Göttingen, Germany). The measurement utilized a Zeiss EC Epiplan Neofluar 5x and 10x BD objective lens. Additionally,

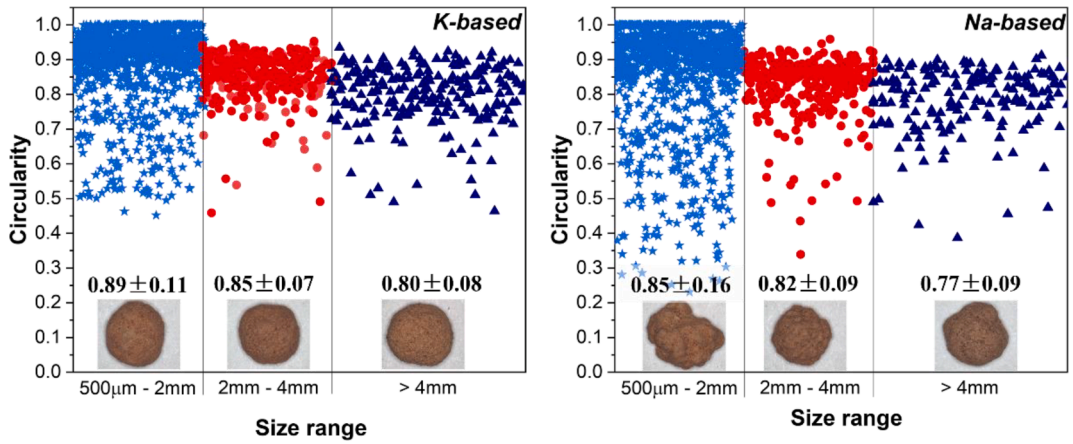

Fig. 5. Circularity of sodium (Na-based) and potassium (K-based) aggregates within each grain size range together with the average circularity value for each range and standard deviation.

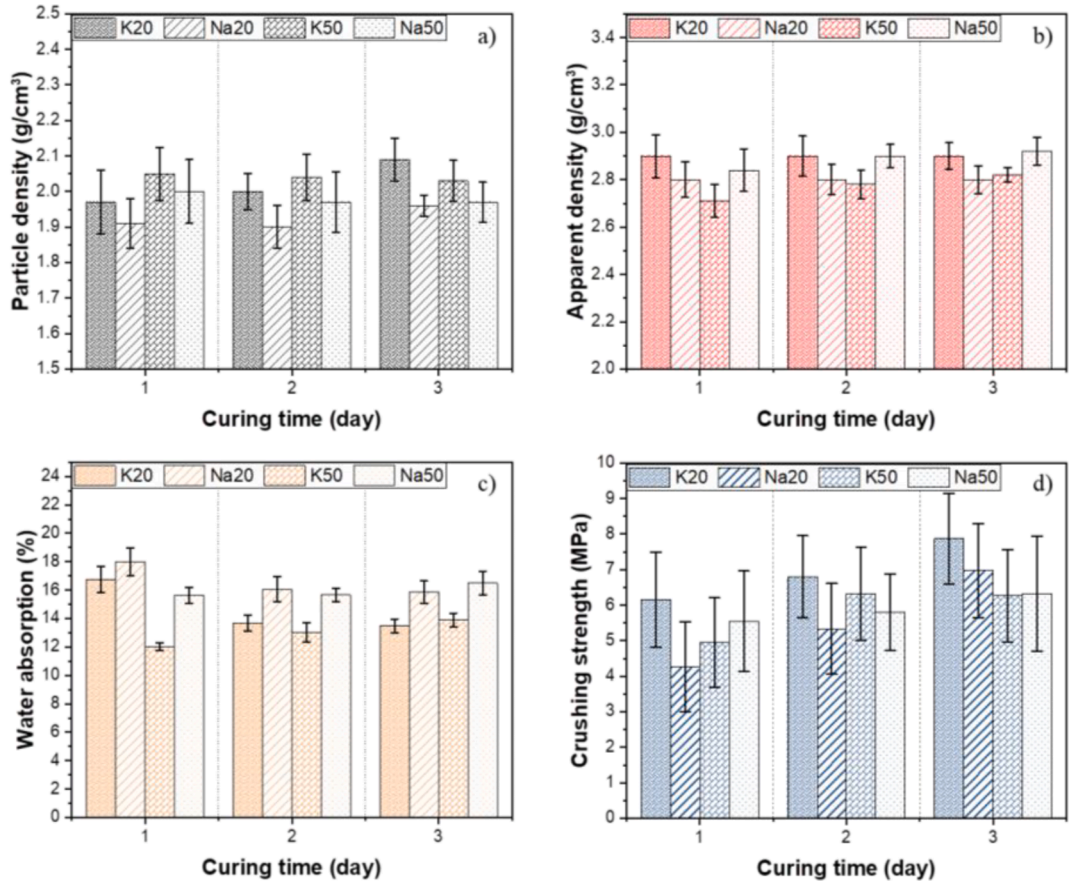

Fig. 6. Particle density, apparent density, water absorption and crushing strength of the designed aggregates. Sample codes are cross-referenced with Table 2. It's noted that error bars represent the deviation, calculated using Student's t-distribution, based on 15 samples for each formulation.

scanning electron microscopy (SEM) investigation was carried out using a Phenom ProX scanning electron microscope equipped with a back-scattered electron (BSD) detector. The samples were sputtered with gold (Emitech K550X sputter coater) at a current of 40 mA for 40 s.

Images of various aggregate fractions (0.5–2 mm, 2–4 mm, and > 4 mm) were processed and analyzed using the free image processing software ImageJ. The regularity of aggregate shape was evaluated using the circularity factor, defined as

$$C = \frac{4\pi S}{P^2} \tag{4}$$

where S denotes grain surface area and P denotes grain perimeter [48,49].

Contour microscopy was employed to determine the linear change of aggregates during heating up to 1000 °C. Images were captured at 100 °C intervals and analyzed using ImageJ. For both types of aggregates, five grains were analyzed, and eight reference lines were selected on each photograph to observe the changes.

Thermogravimetric Analysis (TGA): The thermal behavior of the two types of aggregates was examined using a Thermogravimetric Analyzer (TA TGA500 STA F1 Jupiter). The temperature was measured between

Table 4
Open pore volume calculated from particle density and apparent density.

Curing time (day)	K20	Na20	K50	Na50
1	32.1	31.8	24.4	29.6
2	31.0	32.1	26.6	32.1
3	27.9	30.0	28.0	32.5

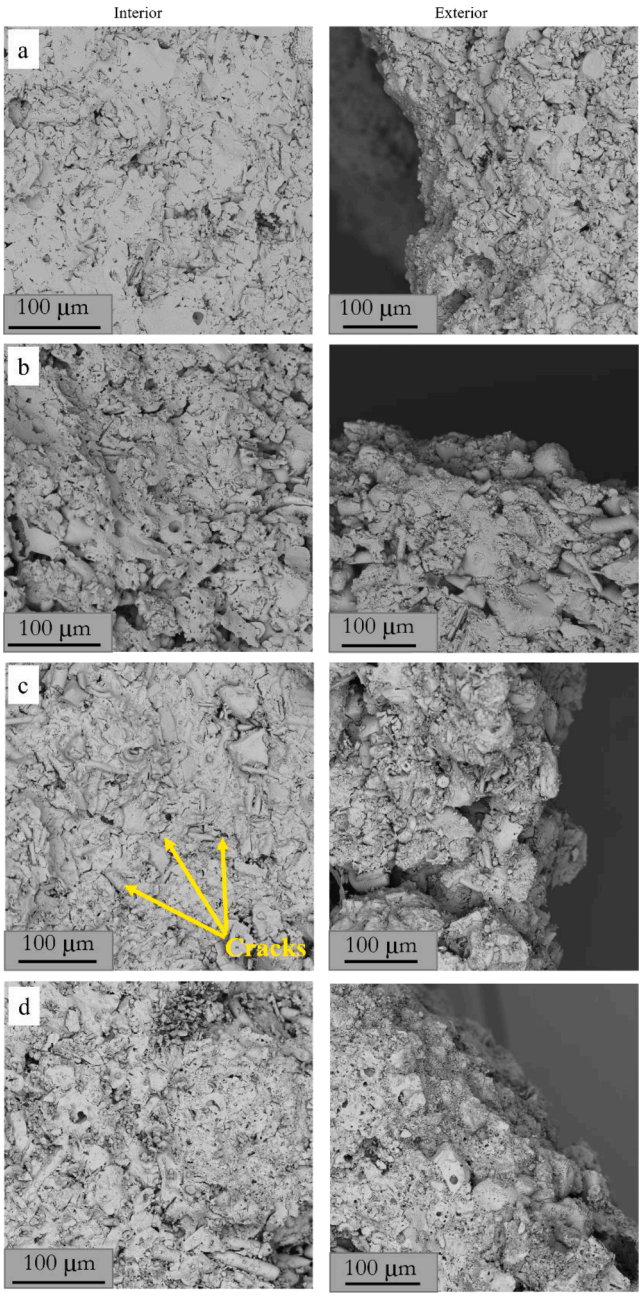

Fig. 7. SEM of four aggregates samples after 3 days curing a) K20-3; b) Na20-3; c) K50-3; d) Na50-3.

40 and 1000 °C at a heating rate of 10 °C/min under a nitrogen environment with a flow rate of 20 ml/min.

2.3.2. Characterization of geopolymer mortars

Geopolymer mortars were subjected to high-temperature testing after 28 days of curing. Utilizing a muffle furnace, three samples from each mix were gradually heated from room temperature to 1000 °C, employing a heating rate of 10 °C per minute. Subsequently, the specimens were exposed to the desired temperature for a period of 1 h.

The structure and distribution of aggregates within the geopolymeric matrix were examined using a ZEISS Axio Imager paired with a ZEISS Axiocam 305 CAMERA Colour, Z2 optical microscope from Carl Zeiss, located in Göttingen, Germany. The analysis employed Zeiss EC Epiplan Neofluar 5x and 10x BD objective lenses. Additionally, scanning electron microscopy (SEM) was conducted using a Phenom ProX scanning electron microscope equipped with a backscattered electron (BSD) detector. Prior to imaging, the samples were coated with a thin layer of gold using an Emitech K550X sputter coater at a current of 40 mA for a duration of 40 s.

The volumetric changes on the prisms were measured and represented as a percentage volume change before and after high-temperature exposure. The data are an average of three measurements per mix and temperature setting, taken with a digital calliper to determine the three dimensions of each prism.

To assess the mechanical performance of the geopolymer mortars, both pre and post high-temperature exposure, the average values were computed using three samples for flexural strength and six test results for compressive strength, according to the EN 196–1 standard [51].

3. Results and discussion

3.1. Shape analysis

The aggregate morphology has a significant influence on the workability, mechanical properties and durability of concrete materials [52]. In this study, two categories of the obtained aggregates are investigated for the shape analysis, differing in activator used, i.e. sodium and potassium. Firstly, qualitative analysis is performed using an optical microscope. Furthermore, as one of the most important indicators of aggregate morphology, the circularity C (Eq. (4) of the aggregates is quantitatively determined by using ImageJ based on optical microscopy images. This parameter indicates the regularity of the shape, for which 1 is a perfect spherical shape and 0 is strongly irregular. The appearance of the exemplary grains as well as the circularity results for the three selected size ranges are summarized in Fig. 5.

The main observation concerning the grain shape is that the sodium-based aggregates are much more irregular than aggregates with potassium-based activator. More specifically, the most irregular fraction with the largest circularity variation is observed within the smallest analyzed range (0.5–2 mm), in particular for Na-based samples. It should be noted that in this particle size range, the dominant part is located between circularity factors 0.9 and 1.0. Further, it is clear to observe that the circularity is reduced in the larger size fraction. This confirms the relation between particle size and circularity, as reported by Wang et al. [49] that the regularity of their shape decreases with the increase in grain size. Moreover, K-based material grains in each range oscillate between 0.5 and 1.0 while Na-based material exhibits a larger circularity range between 0.2 and 1.0. It can therefore be confirmed that a greater irregularity in all size ranges is obtained for aggregates based on the sodium activator. This is mainly due to, despite maintaining the same activator parameters, the obtained Na-based activating solution (0.16 Pa·s) are much more viscous than K-based solution (0.05 Pa·s), leading to a faster agglomeration (growing) of the grains during the preparation, and hence a more irregular shape is obtained. Furthermore, the rough surface generates a stronger bond between the paste and the aggregate, creating a higher paste-aggregate strength [53].

3.2. Particle density, water absorption and crushing strength

Fig. 6a depicts particle density, whereas apparent density (Fig. 6b) represents impermeable grain density. Overall, it can be concluded that changes within particle density are negligible, due to the use of sintering as a step following low temperature 20 or 50 °C pre-curing, oscillating in

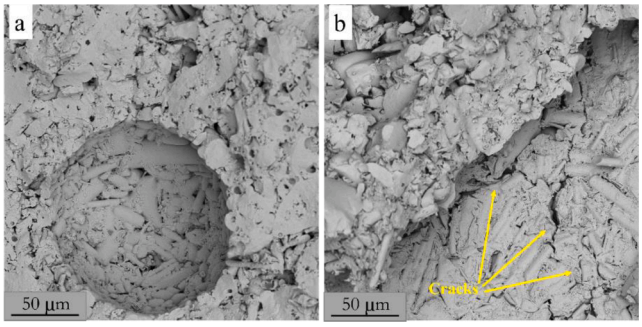

Fig. 8. Interior of potassium-based aggregates a) K20-3; b) K50-3.

a narrow range of the limit value (2.0 g/cm^3) for lightweight and normal aggregates. The pre-curing step is the only difference between aggregates based on the same type of activator (Na or K), thus the analysis that follows is primarily concerned with determining the causes of variations in the sample parameters as a function of time (1 to 3 days) and temperature (20 or 50 °C). An increase in density is observed for samples pre-treated at 20 °C, along with an extension of conditioning time from one to three days, which may indicate a reduction in grain porosity without changing the binder gel structure, as evidenced by the similar value of the skeleton density. Regardless of temperature, sodium aggregates are less dense, which is related to the previously discussed phenomenon of the rapid growth of grains by agglomeration of smaller particles, resulting in reduced packing density with entrapped pores. Open porosity values can be calculated using the particle density and apparent density (Table 4). It is evident that as the curing time is increased at room temperature, the volume of open pores available for the penetrating medium (water) decreases, whereas at 50° C increases. Noteworthy, the skeleton density value of potassium-based aggregates is reduced when the pre-curing temperature changed from 20 °C to 50 °C, hence showing the higher sensitivity of the potassium-based system on the conditioning temperature.

The crushing strength at different curing ages is shown in Fig. 6d. It can be seen that the crushing strength of the 20 °C cured samples developed fast at an early age and then gradually improved with time. However, for 50 °C cured samples, only a minor improvement (Na50-3) or even a decrease (K50-3) with increasing time is noticeable. Here, the strength evolution correlates well with water absorption. It is hypothesized that the defects and deformation after pre-curing have a direct impact on the performance of aggregates after 800 °C sintering. Conversely, the particle densification process under 20 °C from 1 to 3 days further contributes to the higher strength.

3.3. Microstructure

In order to study the microstructure of the aggregates, the SEM micrographs of the different aggregates are collected. The analysis aims to provide insight into the role of pre-curing temperature and alkali activation on microstructure development. Thus, the interior of the grain and the grains' surface of 3 days of curing samples are compared, and the the micrographs after 1 and 2 days curing are presented in Appendix (Fig. A1). Note that these grains have been fired at 800 °C for 2 h subsequently to curing. As shown in Fig. 7, a general examination of the aggregates' cross-section reveals a dense film, demonstrating the bonding development in the aggregate preparation process. Furthermore, it appears that K-activated samples have the most homogenous and dense structure with a visibly smooth appearance, whereas sodium-based samples, particularly Na50-3, appear to be more granular and loosely packed (Fig. 7d).

Overall, all aggregates possess a significant surface roughness and irregularity. Unreacted particles and voids are observed in all aggregates, which impact their performance. Unreacted particles in grains and voids are observed in all aggregates, which impact their performance. Furthermore, within the compacted binder, the mineral wool fibres covered with the gel are observed, which reveals the nature of the raw material after milling, namely fine material containing short chopped fibres. In terms of the effect of pre-curing temperature, the intriguing observation concerning 50 °C cured samples (Fig. 7c, d) indicates that, despite the sufficient binding within the core part, the surface appears to be more porous as compared to 20 °C cured samples, consisting of an insufficient amount of binder to produce a homogeneous structure. This is possibly due to the rapid water loss during pre-curing at 50 °C, which hinders the reaction product formation and good gel development at the surface. Moreover, from the inner structure of K-based samples shown in Fig. 8, increasing microcracks arise in samples cured at 50 °C (Fig. 7c). The present structural deterioration, namely the spaces between unreacted particles on the surface of aggregates as well as the microcracks and trapped air voids within the aggregates causes an increase in the amount of water absorption and deterioration of mechanical strength for high-temperature pre-cured samples.

When comparing the samples based on different types of activators, Na based sample (Fig. 7b, d) shows a greater number of pores than K based system. This phenomenon is suggested to arise from the varied viscosity between different activator types. As evidenced by the shape analysis in Section 3.1, the higher viscosity of the Na-based activator inevitably results in a more irregular particle shape, giving rise to a coarser inner microstructure with more pores and voids.

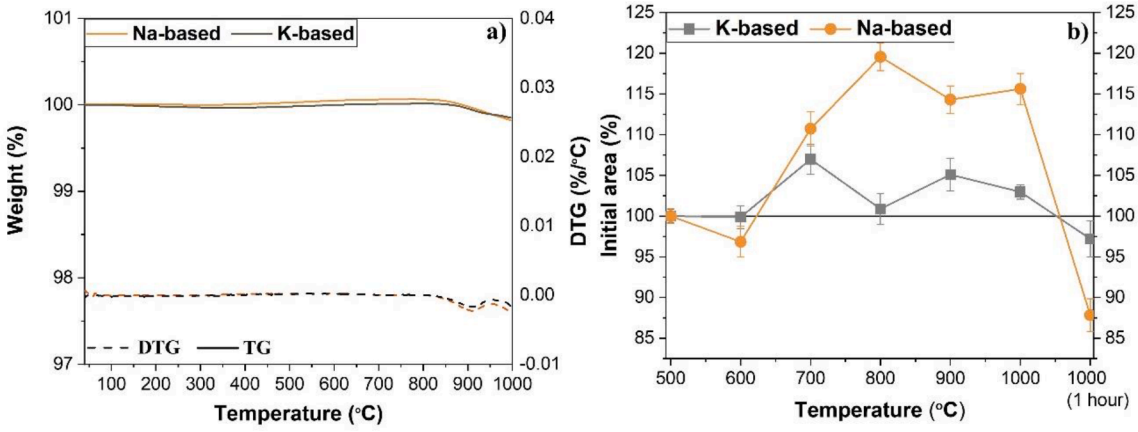

Fig. 9. A) thermogravimetry analysis: tg and dtg curves of aggregates; b) grain area analysis via contour microscopy normalize to area at 500 °C.

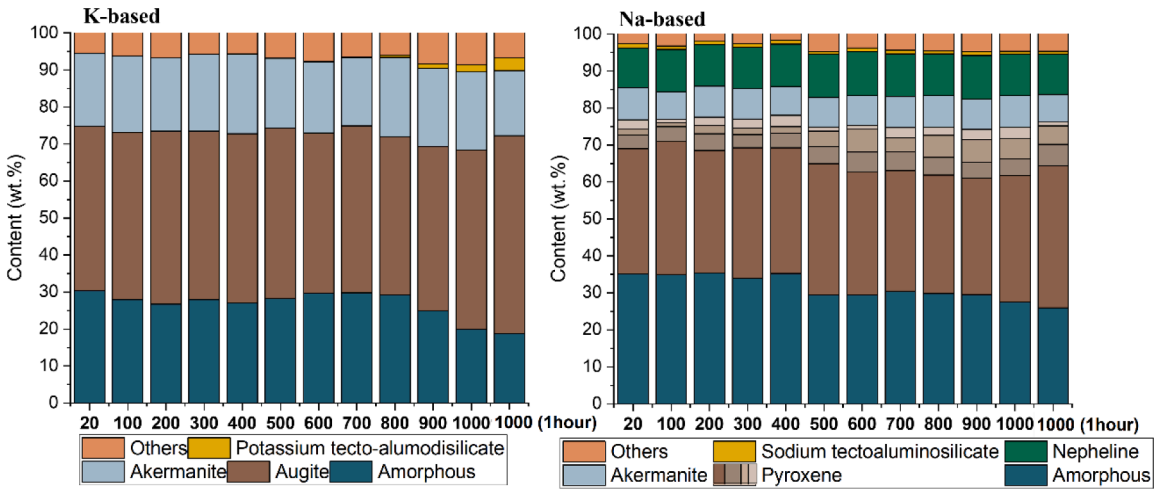

Fig. 10. In-situ high-temperature XRD quantification of potassium and sodium-based aggregates. Note: Sodium tectoaluminosilicate $NaAlSiO_4$; Potassium tectoaluminodisilicate $KAlSi_2O_6$.

Table 5
Factsage thermodynamic calculation of phase distribution at 800 °C for 2 wt% silica added (normalized to 100 wt%).

	K-based wt.%	Na-based wt.%
Clinopyroxene	45	58
Melilite	20	13
Spinel	13	11
Ilmenite	5	5
Leucite	16	5
Nepheline	0	18
Olivine	1	1

3.4. Thermal stability

Based on the characteristics of aggregates at room temperature, such as water absorption and single crushing strength, K20-3 and Na20-3 samples are considered to be the optimal performing designs. Furthermore, from the energy consumption perspective, it is profitable to avoid an elevated pre-curing temperature. Therefore, thermal analysis is performed on two selected types of aggregates, namely K20-3 and Na20-3.

Thermogravimetric analysis is performed under a nitrogen atmosphere to test the stability of the matrix from room temperature to 1000 °C (Fig. 9a). Overall, a relatively low-temperature treatment (800 °C 2 h) provides the material with high stability up to a temperature of 1000 °C, achieving a mass loss of 0.18%, and 0.15% for Na and K-based samples respectively. The DTG curve reflects the curing regime of conditioning of aggregates, where no significant changes are observed until 800 °C while a decrease in mass is noticed after 900 °C. This is related to the thermal treatment of industrial mineral-wool waste that results in the formation of a wide variety of pyrolysis products both in an inert atmosphere and in the air [54]. As the temperature increases, the surface of the solid sample gradually releases pyrolysis gas, reflected by a loss of weight in DTG.

The volumetric stability of aggregates at high temperatures is further analysed via in-situ grain size measurement during heating to a temperature of 1000 °C. An important aspect is that different degree of thermal expansion is observed in both types of grains at or above the temperature of sintering (Fig. 9b). In Na-based aggregates, two significant expansion regions can be distinguished, with the maxima at 800 °C and 1000 °C, followed by an area decrease due to melting. While potassium-based materials are more thermally stable, with a less noticeable expansion above 800 °C and modest shrinkage at 800 and 1000 °C. The contraction event in K-based can be linked to the crystallization at 800 °C and melting at 1000 °C.

In order to explain the different thermal-induced volumetric change phenomena between Na and K-based samples, a quantitative in-situ XRD analysis was performed (Fig. 10) to reveal the phase transformation in the K_2O-Na_2O-CaO-MgO-Al_2O_3-SiO_2 system at high temperatures. The XRD diffractograms are attached in Appendix (Fig. B1). Considering that the material consists of pulverized mineral wool waste, with either potassium or sodium-based alkali activator, all others can be regarded as being the same. MWW is almost entirely glassy as a raw material, and only part of the glass reacts upon alkaline activation. The resulting product is a geopolymer gel with residual glass. It is noted in Fig. 10 that in K-based aggregates no phase changes occur until 800 °C, when K-feldspar appears at the expense of the amorphous phase. At 1000 °C, pyroxene (augite) content increases. In the Na-based system, the pyroxene seems to increasingly form from 400 °C at the expense of amorphous. The higher proportion of the amorphous phase in Na-based systems additionally poses a negative influence on the grain volumetric stability, which is prone to melting and losing shape at elevated temperatures. The majority of the iron in the MWW raw material is divalent, with some being trivalent. Glass and geopolymer behave differently when heated for two hours at 800 °C. The amorphous compound in Fig. 10 may represent the remaining original MWW glass with negligible reactivity and amorphous alkali-activated gel which is expected to be reactive.

The combination of FactSage calculations [55] and experimental observations provided a deeper understanding of the equilibrium phase assemblages and mineralogical composition of the samples. By leveraging FactSage's thermodynamic calculations, it was possible to predict the phase proportions under various conditions, aiding in the interpretation of the experimental results. Table 5 displays the phase proportions of melilite (akermanite $Ca(Mg,Fe)_3Si_2O_7$) and clinopyroxene (augite $Ca(Fe,Mg)Si_2O_6$) in the FactSage calculations that were best reproduced by incorporating 2 wt% SiO_2 via alkali activator solution. This agreement between the calculated (Table 5) and observed phase proportions (Fig. 10) suggests the validity and reliability of the FactSage predictions. The presence of an amorphous phase in the samples can be attributed to the MWW-glass that remained inactivated during pre-curing at lower temperatures. However, it is worth noting that this amorphous phase may also contain alkali-rich residues, which could serve as precursors for the subsequent formation of clinopyroxene and melilite. This observation raises interesting questions about the role of alkali residues in the crystallization process and their influence on the final mineralogical composition. During the production of the aggregate, no equilibrium phase assemblage was established, indicating that local equilibrium had already been attained during the earlier aggregate

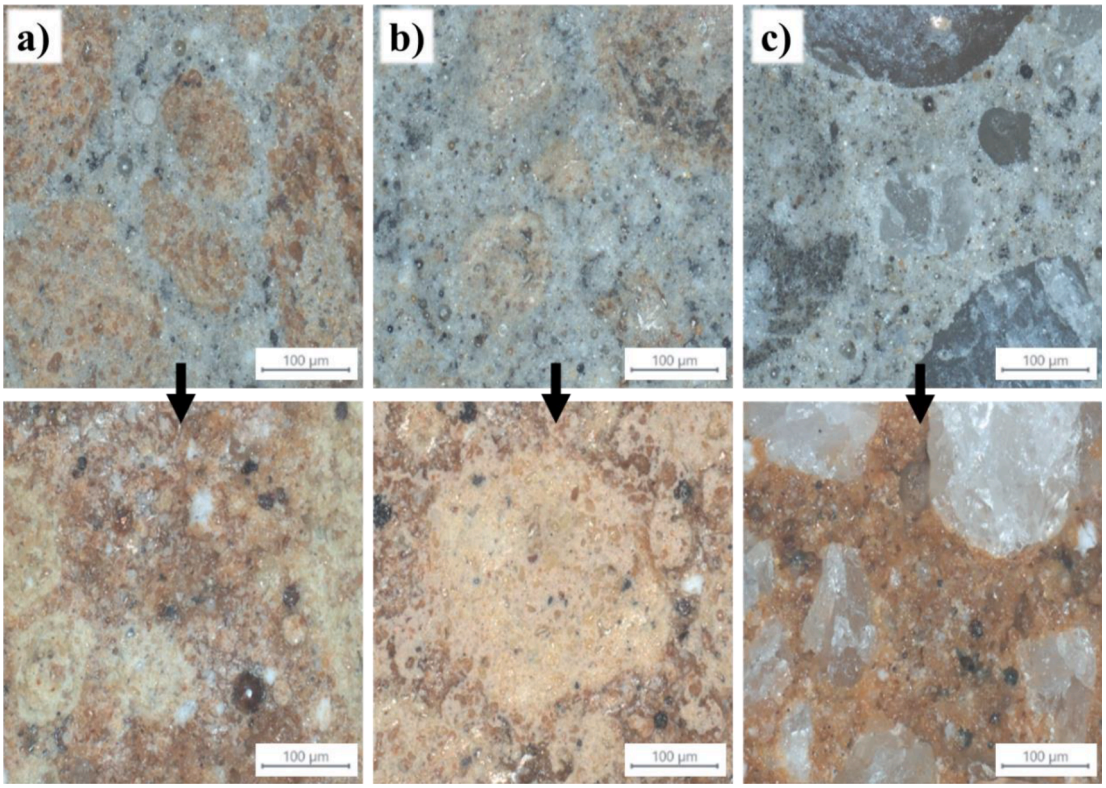

Fig. 11. Cross section of geopolymer mortars before and after high-temperature exposure containing a) K-based; Na-based; c) sand aggregates. Note:Top images at room temperature bottom after exposure to 1000 °C and cooled in air.

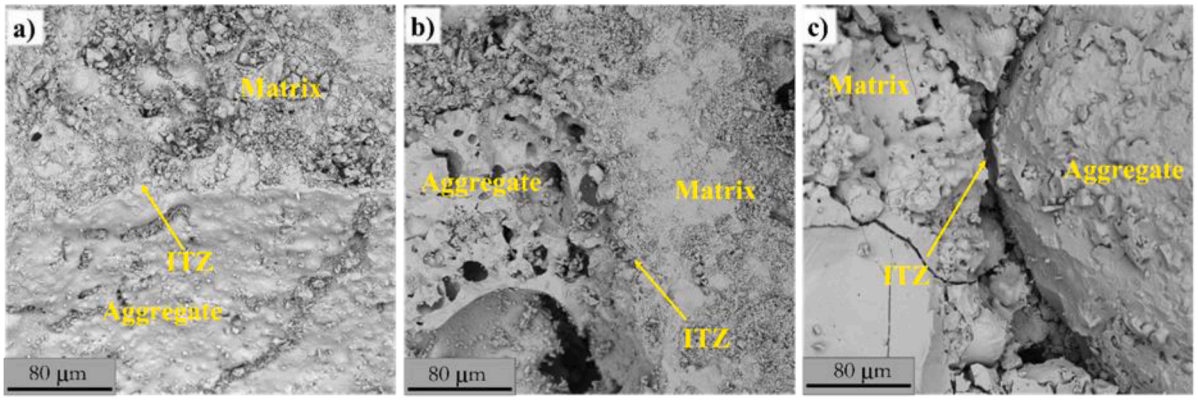

Fig. 12. SEM images of the ITZ after exposure to 1000 °C of a) K-based; b) Na-based and c) sand.

Table 6
Bulk density of geopolymer at room and high temperature together with calculated volume change after thermal exposure.

Sample code	Density at 20 °C (g/cm^3)	Density after 1000 °C (g/cm^3)	Thermal volumetric change $\Delta v/v_0$ (%)
K-based	1.68	1.70	−3.0
Na-based	1.64	1.69	−4.35
Sand	1.90	1.90	−0.75

preparation stage at 800 °C. Consequently, the composition remained relatively stable during subsequent reheating until reaching 800 °C. This finding suggests that the initial treatment at 800 °C played a crucial role in establishing the initial mineralogical composition, which was maintained throughout the subsequent heating steps.

At temperatures above 800 °C, the systems underwent further reactions, leading to the establishment of equilibrium. The decrease in the amorphous phase and the concurrent formation of melilite, clinopyroxene, and K-tectosilicate highlight the dynamic nature of the system. The challenge in crystallizing the K-tectosilicate phase, which requires a specific arrangement of SiO_4 tetrahedra in a three-dimensional structure, indicates the intricate nature of its formation process. Remarkably, at 800 °C, the potassium-based phases remained in the amorphous state, while the sodium-based system exhibited a mineralogical composition consistent with the FactSage calculations. The predominance of pyroxene, nepheline, and akermanite in the sodium-based system further emphasizes the accuracy of the computational predictions. However, it is essential to acknowledge the discrepancy between the experimental observations and the FactSage predictions regarding the formation of spinel. Despite the anticipated formation of spinel according to the computational model, its absence in the experimental system suggests the existence of kinetic hindrances or

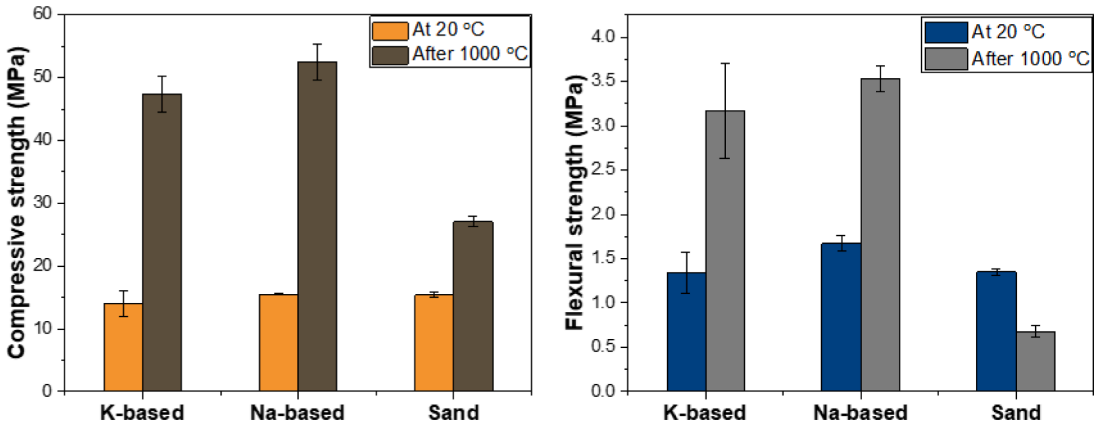

Fig. 13. Compressive and flexural strength of geopolymer samples before and after high-temperature exposure.

Table 7
Mechanical performance of geopolymeric composites after exposure to high temperature.

Aggregate type	Binder	Exposure Temperature (°C)	Gain Compressive strength gain (%)	Ref.
River sand (1:2)	Fly ash	1000	36	[65]
River sand (1:1)	Fly ash	1000	33	
Copper slag (1:2)	Fly ash	1000	59	
Copper slag (1:1)	Fly ash	1000	38	
Silica sand	Metakaolin + Slag	800	−65	[66]
River sand	Metakaolin + Slag	800	−78	
Sandstone	Metakaolin + Slag	800	−97	
Waste concrete sand	Metakaolin + Slag	800	N/A failure	
Basalt sand	Metakaolin + Slag	800	−62	
Rilem sand	Metakaolin + Slag	800	−85	
Basalt	Fly ash	800	−71	[28]
K-based MWW	**Fly ash**	**1000**	**240**	**This study**
Na-based MWW	**Fly ash**	**1000**	**238**	
Sand	**Fly ash**	**1000**	**76**	

other factors that were not accounted for in the calculations. This discrepancy presents an opportunity for further investigation into the factors influencing spinel formation kinetics and the potential limitations of the current thermodynamic model.

The combination of FactSage calculations with experimental observations demonstrates the complementary nature of theoretical predictions and empirical data. While FactSage offers valuable insights into thermodynamic properties and equilibrium phase assemblages, experimental observations provide crucial validation and highlight the complexities beyond thermodynamics, such as kinetic limitations and the influence of precursor residues. These findings contribute to the broader understanding of the system's behavior and offer directions for future research. Exploring the kinetics of spinel formation and investigating the role of alkali residues in crystallization processes could lead to a more comprehensive understanding of the system's dynamics and inform the development of optimized production methods for desired mineralogical compositions.

3.5. Characterization of geopolymer mortar with artificial aggregates

Up to now, the study regarding composite properties with alkali-activated aggregates is still relatively limited and requires further investigation [20]. In this study, two selected groups of aggregates, NA20-3 and K20-3 as presented in *Section 3.2*, are further incorporated into siliceous fly ash-based geopolymer mortar. The behaviour of reinforced composites under both room- and high-temperature conditions (1000 °C) is further compared to a reference sample with normal sand aggregate. The high-temperature exposure test conditions are set as the same as for the aggregates testing, thus from room temperature to 1000 °C at a heating rate of 10 °C/min, and then held at 1000 °C for the duration of 1 h. Above all, the fundamental parameters such as flexural and compressive strength at room and high temperatures, density, thermal shrinkage, and interfacial transition zone (ITZ) after high-temperature exposure are investigated.

3.5.1. Appearance and ITZ evaluation of heated geopolymer mortar

Fig. 11 depicts the cross-section of the matrix before and after high-temperature exposure. In Fig. 11a, b, before being exposed to elevated temperature, the white and grey regions indicate binder gel, and yellow grains denote artificial aggregates. While the paste-aggregate interface is indistinct in colour for sand-contained geopolymer mortar (Fig. 12c). It is widely reported that an alkali activation system can largely improve the ITZ between geopolymeric binder and artificial aggregates [20]. In this work, all mixtures show a dense ITZ, and the aggregates are uniformly distributed, with no evidence of separation or agglomeration, indicating a feasible mix design. After elevated temperature exposure, it is obvious that the colour of the paste binder changes from grey to brownish orange as a result of the iron oxidation from Fe^{2+} to Fe^{3+} [56]. Furthermore, the colour of the aggregates is lightened to be more yellowish, which was also observed after the high-temperature contour microscopy examination as the result of the oxidation reactions mentioned above.

In order to learn the thermally induced deformation in ITZ in more detail, SEM analysis is carried out to samples after exposure to 1000 °C. As shown in Fig. 12, it is obvious that the ITZ of potassium and sodium-based aggregates is denser than that of sand after high-temperature exposure. In artificial aggregates reinforced geopolymer mortars as seen in Fig. 12a,b, the ITZ after being subjected to high temperature is almost indistinguishable. This has resulted from a similar binding system, namely alkali activation, and the unreacted precursor on the aggregate surface tends to react with a binder, leading to the formation of mechanical interlocking on the porous, rough surface of aggregates [20]. Additionally, the sintering reaction among the fly ash-based binder and artificial aggregates above 600 °C further promotes the binding and strengthens the ITZ [57]. In terms of normal sand aggregates, a conversion takes place at a temperature of 573 °C when α-quartz undergoes

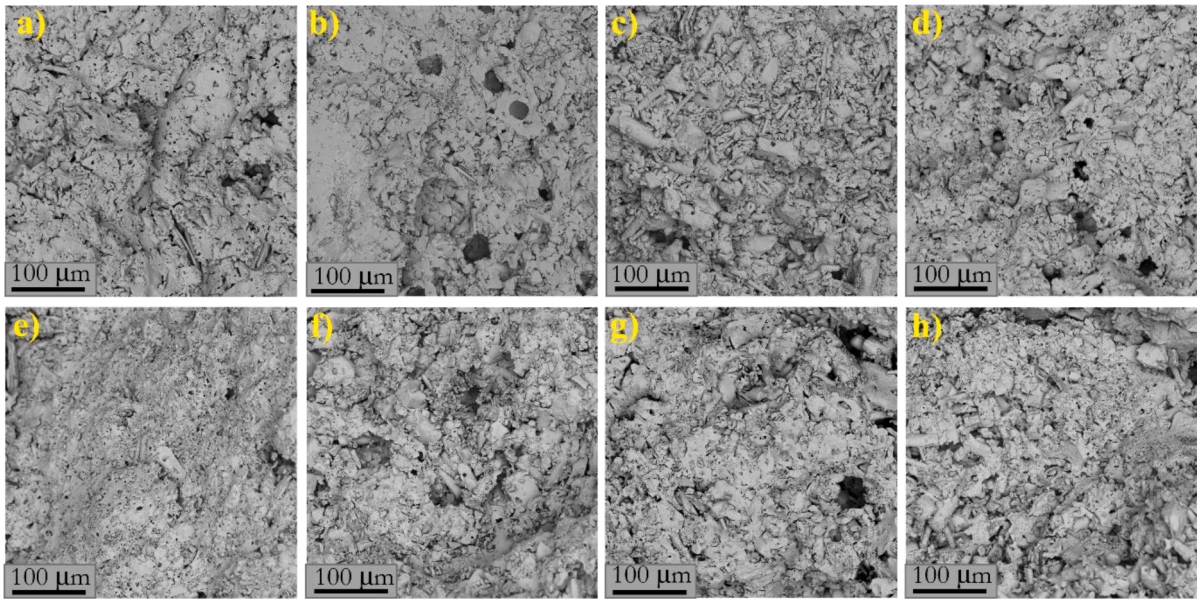

Fig. A. SEM pictures of aggregates core part. a) K20-1; b) K20-2; c) Na20-1; d) Na20-2; e) K50-1; f) K50-2; g) Na50-1; h) Na50-2.

a reversible change in its crystal structure to form β-quartz and causes a linear expansion, while during cooling the change is reversed from β- to α-quartz and shrinks [58]. Due to the reversible thermal expansion and shrinkage of sand aggregates at high temperatures, an obvious gap is observed between the grain and paste.

3.5.2. *Volumetric stability and density evolution*

Aggregate performance inside an alkaline matrix might be unpredictable, even with knowledge of their thermal response in an oxidising environment and using literature information of paste behaviour during heating [57]. The processes that direct volume change are inextricably linked to reaching the glass transition and further melting temperature. As a transitional state between glass and liquid, the glassy phase becomes more plastic above the sintering temperature. These changes are observed as swelling in the air, but the fly ash-based geopolymer, also possesses its own response to high temperature, namely shrinkage, densification and sintering at 1000 °C [59]. As a result, the observed change in geometry is an indicator of the grain's stability under high-temperature conditions, which explains the observed shrinkage caused by the aforementioned phenomena. As discussed above, the more vitreous phase presented in the Na-based aggregate has a more detrimental effect on the grain performance. In terms of the thermal behaviour of the binder, the applied geopolymeric binder contains a potassium activator, hence the softening temperature is expected to be around 800 °C [57,60]. Furthermore, all samples begin to shrink significantly above the softening temperature due to the matrix sintering. For the thermal behaviour of aggregates, as learned above, the applied sodium and potassium aggregates show expansion above 700 °C (Fig. 9b), respectively, while sand expands at 573 °C.

The paste melting and aggregate thermal expansion mechanisms overlap and pose a coupling effect on composite high-temperature stability. As can be observed in Table 6, all composites exhibit a much lower thermal volumetric change than that of pure geopolymer paste at 1000 °C (~8%) [61]. However, the thermal shrinkage is significantly smaller when sand aggregate is employed. This is because the sand aggregates have high stiffness, which could act as a strong skeleton under high temperatures that largely offsets the matrix shrinkage. Nevertheless, owing to the drastic competition between the binder shrinkage and the thermal expansion of sand aggregates, severe structural deterioration like holes and cracks are obtained in the composite with sand as shown in Fig. 12c. The irreparable damage and gaps developed between the aggregate and the paste, causing problems with the material's use after high-temperature exposure.

Noteworthy, on the other hand, both artificial aggregates have an improved binding within the alkali activated matrix due to the presence of unreacted precursor on the particle surface. On the other hand, as discussed above, the artificial aggregates show a geopolymer alike thermal behaviour due to the similar chemical composition, sintering and/or melting after 800 °C along with geopolymeric binder, which further weakens the competition mechanism between binder and aggregates. As a result, the matrix is largely preserved with less thermal deterioration after being subjected to elevated temperature as evidenced by SEM analysis in Fig. 12a, b. In conclusion, selecting potassium aggregates with better thermal stability (lower thermal expansion value) further poses a positive impact on geopolymer mortar performance at high temperatures than sodium aggregates.

3.5.3. *Compressive and flexural strength before and after high temperature-exposure*

Fig. 13 further compares the compressive and flexural strength before and after high-temperature exposure. The consistent and marginal variance in mechanical strength, varying from 14 to 15.5 MPa, among the three geopolymer mortars when tested at room temperature, unequivocally demonstrates the feasibility of utilizing specially designed artificial aggregates as a suitable alternative to traditional sand aggregates The geopolymer mortars with sodium-based aggregates and sand aggregates show slightly higher flexural and compressive strength than those of the geopolymer mortars with potassium-based aggregates, indicating the suitability of replacing normal sand with the designed artificial aggregates. An interesting phenomenon is related to the lower single-crushing strength of sodium-based aggregates (Fig. 6) but higher geopolymer mortar strength results. This difference is mainly related to the shape variation of the aggregate grains. It is widely known the mechanical strength of composites not only depends on the aggregate crushing strength but also is largely influenced by the binder gel-aggregate binding capabilities [43]. As investigated in *Section 3.1*, the sodium-based aggregate and sand are more irregular in shape than the potassium-based aggregate, which contributes to a higher adherence force between binder and aggregates [62,63], and gives rise to a larger mechanical strength. In addition, as compared to sand, the sodium-based aggregates are believed to further react with the geopolymer binder and adhere to the binder, hence providing a better bonding,

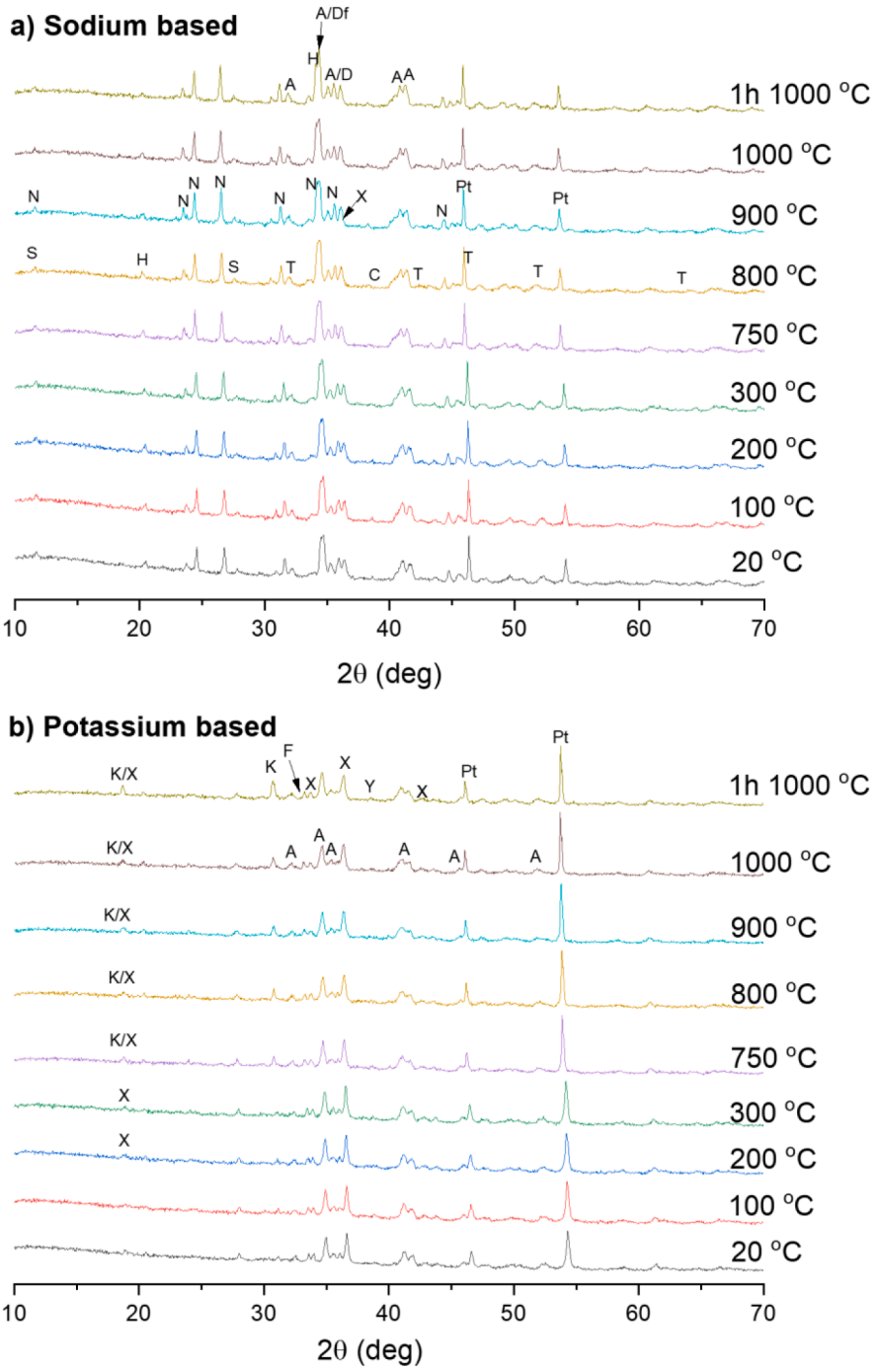

Fig. B. XRD diffractograms of in-situ high-temperature XRD (selected sample data) a) sodium-based. b) potassium-based Legend: **N**-Nepheline; **X**-Akermanite; **S**-Sodium-tectoaluminosilicate; **K**-Potassium aluminosilicate; **A**-Augite; **Pt**-Platinum; **D**-Diopside; **Df**-Diopside ferran; **T**-Rutile; **H**-Ammonium sulphite; **C**-Calcium magnesium nitrate; **F**-Potaassium iron phosphate; **Y**-Perovskite.

resulting in the highest compressive and flexural strength at room temperature.

After exposure to a high temperature, it is clear that geopolymer mortars reinforced with artificial aggregates and normal sand exhibit different mechanical strength evolution patterns. The artificial aggregates reinforced samples experience a significant gain in both compressive and flexural strength. While sand-incorporated geopolymer mortar has an obviously lower compressive strength gain (Table 7) and the flexural strength is significantly reduced after high-temperature exposure. It is reported by Lahoti et al. [27,64] that the compressive strength of geopolymer-based materials after high-temperature exposure is mainly governed by competing mechanisms of crack formation, matrix densification and viscous sintering. In our case, the matrix densification and viscous sintering play a dominant role over crack formation in determining the compressive strength, resulting in a strength gain for all samples. For geopolymer mortar with artificial aggregates, as learned by SEM analysis, the geopolymeric behavior observed in artificial aggregates under elevated temperature largely mitigates the thermal incompatibility within geopolymer mortar, reducing the matrix deterioration., the drastic thermal mismatch between sand and geopolymer binder leads to severe structural deterioration and cracking in the sample with sand aggregates as described

above. Thus, the strength gain effect is weakened in sand geopolymer mortar, resulting in the lowest compressive strength gain after high-temperature exposure. This negative effect of structural deterioration in sand-incorporated samples is more significant in flexural strength evolution, since the flexural property of material is largely affected by crack formation. As a result, a halved flexural strength is obtained in the sand-involved sample after high-temperature exposure. When comparing the sample with different types of artificial aggregates, the highest residual mechanical performance is obtained in the sample with sodium-based aggregates. As discussed above, the more irregular shape and higher surface roughness of Na-based aggregates provides a larger contact surface for developing an ITZ in geopolymer mortar. This enhanced bonding area with Na-based aggregates further poses a positive influence on thermal–mechanical performance, by strengthening the ITZ during viscous sintering and melting. In this case, the geopolymer mortar with Na-based aggregates exhibits the highest residual mechanical strength after high-temperature exposure.

In conclusion, as compared to normal sand aggregate, the designed artificial aggregates show a geopolymer-alike thermal behaviour, such as re-crystallization, viscous sintering, and melting. The geopolymer-alike thermal behaviour provides artificial aggregates with the advantage over traditional aggregates at elevated temperatures (Table 7), by reducing the thermal mismatch between the geopolymer matrix and the aggregates, which contributes to better microstructural stability and mechanical performance subjected to high temperatures. The varied shape in different types of artificial aggregates have a noticeable effect on the mechanical strength of geopolymer mortar at both ambient and elevated temperatures by influencing the binder gel-aggregate binding properties.

4. Conclusions

The objective of this study is to design a sustainable artificial aggregate solely based on mineral wool waste, with the special focus on high-temperature application. Overall, the proposed method shows that mineral wool waste can be a promising raw material for preparing the alkali-activated artificial aggregate with excellent thermal performance. The initial properties, as well as the thermal behaviour of the designed artificial aggregate, are determined and the optimum preparation regime is proposed. The designed artificial aggregates are further applied to prepare geopolymer-based composite, and their performances are compared with that of normal sand-incorporated geopolymer. The following conclusions are the most noteworthy findings:

- To produce the artificial aggregate based on mineral wool waste, a room temperature curing is proposed instead of elevated-temperature pre-curing in considering the energy costs and the structural deterioration with high temperature curing. Regarding the curing time, it is beneficial for strength development to provide 3 days of curing prior to sintering at 800 °C. The obtained artificial aggregates (T = 20 °C, t = 3 days) show particle density ranging from 1960 kg/m^3 to 2090 kg/m^3 and crushing strengths of 7.0 to 7.9 MPa.
- The activator type plays a dominant role in aggregate particle formation. The sodium-based activator with high viscosity leads to a more irregular shape of grains within the analyzed aggregates ranges (from 500 μm to above 4 mm) as well as a coarser microstructure with more pores and air voids. This consequently results in a lower particle density, higher water absorption and lower crushing strength as compared to potassium-based aggregate.
- High-temperature response of aggregates is strongly related to the alkali cation type. Both aggregate types show a certain degree of thermal expansion; however, in comparison, the expansion is reduced in the potassium-based system, which is mainly related to its high rate of crystallinity.
- As compared to normal sand, artificial aggregates exhibit better compatibility in the geopolymer composite given its comparable chemical composition to geopolymer binder. Under the alkaline environment, a better bonding between the binder and artificial aggregates is achieved, reflected by the development of mechanical interlocking on the porous and rough surface of the aggregates with an indistinguishable interfacial transition zone. As a result, a superior mechanical performance is achieved in geopolymer composite with artificial aggregates.
- At high temperatures, the designed artificial aggregates show a geopolymer-alike thermal behaviour, namely re-crystallization, viscous sintering, and melting. It provides artificial aggregates with the advantage over traditional sand in high-temperature resistant geopolymer concrete, by reducing the thermal mismatch between the geopolymer matrix and the aggregates, thus contributing to better microstructural stability and mechanical performance when subjected to high temperatures.

The findings of this work clarify the possibility of valorizing MWW to prepare alkali-activated artificial aggregate and demonstrate promising practical characteristics for both ambient and high temperature applications. Overall, this work proposes a guideline for further research towards a potential reutilization strategy for MWW in artificial aggregate manufacturing. Nevertheless, further investigation is required to optimize the fabrication process, for instance the viscosity tailoring and sintering energy reduction, by exploring the influence of alkali activator formulation, such as sodium (Na) percentage and silicon-to-sodium (Si/Na) molar ratio.

CRediT authorship contribution statement

K.M. Klima: Writing – original draft, Methodology, Investigation, Formal analysis, Data curation, Conceptualization. **Y. Luo:** Writing – original draft, Methodology, Investigation, Formal analysis, Data curation, Conceptualization. **H.J.H. Brouwers:** Writing – review & editing, Supervision, Project administration, Funding acquisition. **Qingliang Yu:** Writing – review & editing, Supervision, Project administration, Methodology, Funding acquisition, Conceptualization.

Declaration of Competing Interest

The authors declare that they have no known competing financial interests or personal relationships that could have appeared to influence the work reported in this paper.

Data availability

Data will be made available on request.

Acknowledgements

This research was carried out under project number S17013a in the framework of the Partnership Program of the Materials innovation institute M2i (www.m2i.nl), the Technology Foundation TTW, which is part of the Netherlands Organization for Scientific Research (www.nwo.nl) (Project No. 16347), China Scholarship Council (Project No. 201906370011) and the department of the Built Environment at Eindhoven University of Technology. The authors gratefully thank Mr. Andreas Leismann (ROCKWOOL) for the materials supply.

Appendix

.

References

[1] B. Nagy, T.K. Simon, R. Nemes, Effect of built-in mineral wool insulations durability on its thermal and mechanical performance, J. Therm. Anal. Calorim. 139 (1) (2020) 169–181.
[2] N. Voronina, Acoustic properties of fibrous materials, Appl. Acoust. 42 (1994) 165–174, https://doi.org/10.1016/0003-682X(94)90005-1.
[3] O. Väntsi, T. Kärki, Mineral wool waste in Europe: a review of mineral wool waste quantity, quality, and current recycling methods, J. Mater. Cycles Waste Manage. 16 (2014) 62–72.
[4] J. Yliniemi, R. Ramaswamy, T. Luukkonen, O. Laitinen, Á.N. de Sousa, M. Huuhtanen, M. Illikainen, Characterization of mineral wool waste chemical composition, organic resin content and fiber dimensions: aspects for valorization, Waste Manag. 131 (2021) 323–330.
[5] T. Sattler, M. Sartori, R. Galler, R. Pomberger, J. Krainz, J. Schimek, D. Vollprecht, Effects of cement addition and briquetting of rock wool on its geomechanical stability in landfills, Waste Manag. Res. 38 (4) (2020) 408–414.
[6] T. Sattler, R. Pomberger, J. Schimek, D. Vollprecht, Mineral wool waste in austria, associated health aspects and recycling options, Detritus. 9 (2020) 174–180.
[7] J. Pranckevičienė, Impact of mineral wool production waste on properties of sintered ceramics, (2011).
[8] Z. Chen, H. Wang, R. Ji, L. Liu, C. Cheeseman, X. Wang, Reuse of mineral wool waste and recycled glass in ceramic foams, Ceram. Int. 45 (2019) 15057–15064, https://doi.org/10.1016/j.ceramint.2019.04.242.
[9] J. Felegi Jr, K.P. Kehrer, Composite fiberboard and process of manufacture, (1990).
[10] M.H. Ali, Fire resistant gypsum board containing mineral wool fibers and method, (1985).
[11] W.-T. Lin, A.n. Cheng, R. Huang, Y.-C. Wu, T.-Y. Han, Rock wool wastes as a supplementary cementitious material replacement in cement-based composites, Comput. Concr. 11 (2) (2013) 93–104.
[12] W.-T. Lin, T.-Y. Han, C.-C. Huang, A.n. Cheng, R. Huang, Using rock wool wastes as partial replacement of cement in cement-based composites, Adv. Sci. Lett. 8 (1) (2012) 489–494.
[13] A.n. Cheng, W.-T. Lin, R. Huang, Application of rock wool waste in cement-based composites, Mater. Des. 32 (2) (2011) 636–642.
[14] J. Yliniemi, B. Walkley, J.L. Provis, P. Kinnunen, M. Illikainen, Influence of activator type on reaction kinetics, setting time, and compressive strength of alkali-activated mineral wools, J. Therm. Anal. Calorim. 144 (4) (2021) 1129–1138.
[15] J. Yliniemi, B. Walkley, J.L. Provis, P. Kinnunen, M. Illikainen, Nanostructural evolution of alkali-activated mineral wools, Cem. Concr. Compos. 106 (2020), 103472.
[16] J. Yliniemi, P. Kinnunen, P. Karinkanta, M. Illikainen, Utilization of mineral wools as alkali-activated material precursor, Materials. 9 (5) (2016) 312.
[17] P. Kinnunen, J. Yliniemi, B. Talling, M. Illikainen, Rockwool waste in fly ash geopolymer composites, Journal of Material Cycles and Waste, Management 19 (2017) 1220–1227, https://doi.org/10.1007/s10163-016-0514-z.
[18] J. Zhao, L. Tong, B. Li, T. Chen, C. Wang, G. Yang, Y. Zheng, Eco-friendly geopolymer materials: A review of performance improvement, potential application and sustainability assessment, J. Clean. Prod. 307 (2021), 127085, https://doi.org/10.1016/j.jclepro.2021.127085.
[19] L. Pilato (Ed.), Phenolic Resins: A Century of Progress, Springer Berlin Heidelberg, Berlin, Heidelberg, 2010.
[20] P. Ren, T.-C. Ling, K.H. Mo, Recent advances in artificial aggregate production, Recent advances in artificial aggregate production 291 (2021), 125215, https://doi.org/10.1016/j.jclepro.2020.125215.
[21] F. Tajra, M. Abd Elrahman, C. Lehmann, D. Stephan, Properties of lightweight concrete made with core-shell structured lightweight aggregate, Constr. Build. Mater. 205 (2019) 39–51.
[22] A.B. López-García, M. Uceda-Rodríguez, S. León-Gutiérrez, C.J. Cobo-Ceacero, J. M. Moreno-Maroto, Eco-efficient transformation of mineral wool wastes into lightweight aggregates at low firing temperature and associated environmental assessment, Constr. Build. Mater. 345 (2022), 128294, https://doi.org/10.1016/j.conbuildmat.2022.128294.
[23] J.L. Provis, Alkali-activated materials, Cem. Concr. Res. 114 (2018) 40–48.
[24] C.-G. Go, J.-R. Tang, J.-H. Chi, C.-T. Chen, Y.-L. Huang, Fire-resistance property of reinforced lightweight aggregate concrete wall, Constr. Build. Mater. 30 (2012) 725–733.
[25] M. Dener, M. Karatas, M. Mohabbi, High temperature resistance of self compacting alkali activated slag/portland cement composite using lightweight aggregate, Constr. Build. Mater. 290 (2021), 123250.
[26] M.B. Karakoç, Effect of cooling regimes on compressive strength of concrete with lightweight aggregate exposed to high temperature, Constr. Build. Mater. 41 (2013) 21–25.
[27] M. Lahoti, K.H. Tan, E.-H. Yang, A critical review of geopolymer properties for structural fire-resistance applications, Constr. Build. Mater. 221 (2019) 514–526.
[28] D.L.Y. Kong, J.G. Sanjayan, Effect of elevated temperatures on geopolymer paste, mortar and concrete, Cem. Concr. Res. 40 (2) (2010) 334–339.
[29] P. Krivenko, Alkali-activated cements and concretes, (2003).
[30] Z.S. Yap, N.H.A. Khalid, Z. Haron, A. Mohamed, M.M. Tahir, S. Hasyim, A. Saggaff, Waste Mineral Wool and Its Opportunities—A Review, Materials. 14 (2021) 5777.
[31] X. Wang, Y. Jin, Z. Wang, R.B. Mahar, Y. Nie, A research on sintering characteristics and mechanisms of dried sewage sludge, J. Hazard. Mater. 160 (2-3) (2008) 489–494.
[32] A. Ivanič, G. Kravanja, W. Kidess, R. Rudolf, S. Lubej, The influences of moisture on the mechanical, morphological and thermogravimetric properties of mineral wool made from basalt glass fibers, Materials. 13 (2020) 2392.
[33] J. Sjostrom, R.J. Mcnamee, Measuring thermal material properties for structural fire engineering, (2020).
[34] M.M. Smedskjaer, M. Solvang, Y. Yue, Crystallisation behaviour and high-temperature stability of stone wool fibres, J. Eur. Ceram. Soc. 30 (6) (2010) 1287–1295.
[35] M. Pavlin, B. Horvat, A. Frankovič, V. Ducman, Mechanical, microstructural and mineralogical evaluation of alkali-activated waste glass and stone wool, Ceram. Int. 47 (11) (2021) 15102–15113.
[36] L.P. Qian, L.Y. Xu, Y. Alrefaei, T. Wang, T. Ishida, J.G. Dai, Artificial alkali-activated aggregates developed from wastes and by-products: A state-of-the-art review, Resour. Conserv. Recycl. 177 (2022), 105971, https://doi.org/10.1016/j.resconrec.2021.105971.
[37] R. Yu, P. Spiesz, H.J.H. Brouwers, Mix design and properties assessment of ultra-high performance fibre reinforced concrete (UHPFRC), Cem. Concr. Res. 56 (2014) 29–39.
[38] H.J.H. Brouwers, Particle-size distribution and packing fraction of geometric random packings, Phys. Rev. E 74 (2006) 31309.
[39] H.J.H. Brouwers, H.J. Radix, Self-compacting concrete: theoretical and experimental study, Cem. Concr. Res. 35 (11) (2005) 2116–2136.
[40] X. Gao, Q.L. Yu, H.J.H. Brouwers, Assessing the porosity and shrinkage of alkali activated slag-fly ash composites designed applying a packing model, Constr. Build. Mater. 119 (2016) 175–184.
[41] P.H.R. Borges, L.F. Fonseca, V.A. Nunes, T.H. Panzera, C.C. Martuscelli, Andreasen particle packing method on the development of geopolymer concrete for civil engineering, J. Mater. Civ. Eng. 26 (4) (2014) 692–697.
[42] T.S. Ng, S.J. Foster, Development of a mix design methodology for high-performance geopolymer mortars, Struct. Concr. 14 (2) (2013) 148–156.
[43] Yliniemi, Paiva, Ferreira, Tiainen, Illikainen, Illikainen, Development and incorporation of lightweight waste-based geopolymer aggregates in mortar and concrete, Constr. Build. Mater. 131 (2017) 784–792.
[44] ASTM C 128-01, Standard Test Method for Density , Relative Density (Specific Gravity), and Absorption, ASTM International. (2001) 1–6.
[45] F.J. Semel, D.A. Lados, Porosity analysis of PM materials by helium pycnometry, Powder Metall. 49 (2006) 173–182, https://doi.org/10.1179/174329006X95347.
[46] P. Gomathi, A. Sivakumar, Characterization on the strength properties of pelletized fly ash aggregate, ARPN J. Eng. Appl. Sci. 7 (2012) 1523–1532.
[47] K.N. Shivaprasad, B.B. Das, Determination of optimized geopolymerization factors on the properties of pelletized fly ash aggregates, Constr. Build. Mater. 163 (2018) 428–437.
[48] H. Hafid, G. Ovarlez, F. Toussaint, P.H. Jezequel, N. Roussel, Effect of particle morphological parameters on sand grains packing properties and rheology of model mortars, Cem. Concr. Res. 80 (2016) 44–51.
[49] A. Wang, M. Huang, Y. Chu, Y. Zhu, K. Liu, L. Guo, P. Liu, D. Sun, Optimization of mix proportion of basic magnesium sulfate cement-based high-strength coral concrete, Constr. Build. Mater. 341 (2022), 127709.
[50] C.W. Bale, E. Bélisle, P. Chartrand, S.A. Decterov, G. Eriksson, K. Hack, I.-H. Jung, Y.-B. Kang, J. Melançon, A.D. Pelton, C. Robelin, S. Petersen, FactSage thermochemical software and databases — recent developments, Calphad 33 (2009) 295–311, https://doi.org/10.1016/j.calphad.2008.09.009.
[51] BS EN 196-1, Methods of testing cement, Part 1: Determination of Strength. (2005).
[52] P.K. Mehta, P.J.M. Monteiro, Concrete: microstructure, properties, and materials, McGraw-Hill Education, 2014.
[53] B.M. Aïssoun, S.-D. Hwang, K.H. Khayat, Influence of aggregate characteristics on workability of superworkable concrete, Mater. Struct. 49 (1-2) (2016) 597–609.
[54] M.P. Krasnovskih, N.G. Maksimovich, Y.I. Vaisman, A.A. Ketov, Thermal stability of mineral-wool heat-insulating materials, Russ. J. Appl. Chem. 87 (10) (2014) 1430–1434.
[55] C.W. Bale, P. Chartrand, S.A. Degterov, G. Eriksson, K. Hack, R. Ben Mahfoud, J. Melançon, A.D. Pelton, S. Petersen, FactSage thermochemical software and databases, Calphad 26 (2002) 189–228, https://doi.org/10.1016/S0364-5916(02)00035-4.
[56] P.K. Sarker, S. Kelly, Z. Yao, Effect of fire exposure on cracking, spalling and residual strength of fly ash geopolymer concrete, Mater. Des. 63 (2014) 584–592, https://doi.org/10.1016/j.matdes.2014.06.059.
[57] K.M. Klima, K. Schollbach, H.J.H. Brouwers, Q. Yu, Thermal and fire resistance of Class F fly ash based geopolymers–A review, Constr. Build. Mater. 323 (2022), 126529.
[58] J.D. Axe, G. Shirane, Study of the Alpha-Beta Quartz phase transformation by inelastic neutron scattering, Phys. Rev. B 1 (1970) 342–348, https://doi.org/10.1103/PhysRevB.1.342.
[59] E.M. Heuse, G. Partridge, Creep testing of glass-ceramics, J. Mater. Sci. 9 (8) (1974) 1255–1261.
[60] Z. Pan, J.G. Sanjayan, Factors influencing softening temperature and hot-strength of geopolymers, Cem. Concr. Compos. 34 (2012) 261–264, https://doi.org/10.1016/j.cemconcomp.2011.09.019.
[61] K.M. Klima, K. Schollbach, H.J.H. Brouwers, Q. Yu, Enhancing the thermal performance of Class F fly ash-based geopolymer by sodalite, Constr. Build. Mater. 314 (2022), 125574.
[62] H.Z. Cui, T.Y. Lo, S.A. Memon, W. Xu, Effect of lightweight aggregates on the mechanical properties and brittleness of lightweight aggregate concrete, Constr. Build. Mater. 35 (2012) 149–158.
[63] O. Kayali, Fly ash lightweight aggregates in high performance concrete, Constr. Build. Mater. 22 (12) (2008) 2393–2399.

[64] M. Lahoti, S.F. Wijaya, K.H. Tan, E.-H. Yang, Tailoring sodium-based fly ash geopolymers with variegated thermal performance, Cem. Concr. Compos. 107 (2020), 103507, https://doi.org/10.1016/j.cemconcomp.2019.103507.
[65] M. Sivasakthi, R. Jeyalakshmi, N.P. Rajamane, Fly ash geopolymer mortar: Impact of the substitution of river sand by copper slag as a fine aggregate on its thermal resistance properties, J. Clean. Prod. 279 (2021), 123766.
[66] F. Şahin, M. Uysal, O. Canpolat, Systematic evaluation of the aggregate types and properties on metakaolin based geopolymer composites, Constr. Build. Mater. 278 (2021), 122414, https://doi.org/10.1016/j.conbuildmat.2021.122414.